Landmark-based registration of OCT image sequences for the follow-up of stent coverage and apposition

Laurent Sarry, Romain Dumas, Florian Dubuisson, Emilie Pery, Nicolas Combaret, Pascal Motreff

Landmark-based registration of OCT image sequences for the follow-up of stent coverage and apposition

Laurent Sarry[1], Romain Dumas[1], Florian Dubuisson[1], Emilie Péry[1], Nicolas Combaret[2], Pascal Motreff[1,2]

[1]Clermont Université, Université d'Auvergne, ISIT, BP 10448, F-63000 Clermont-Ferrand.
CNRS, UMR6284, BP 10448, F-63000 Clermont-Ferrand.
[2]CHU Gabriel Montpied, Département de Cardiologie, BP 69, F-63003 Clermont-Ferrand.

{laurent.sarry@u-clermont1.fr}

Abstract. We propose a new landmark-based registration method designed to take into account the specific geometry of OCT endovascular acquisition. B-spline approximation is used to recover probe trajectory and angular offsets between two image sequences from a few landmarks pinpointed out by the cardiologist. The well-posedness of the control point estimation is assured by a bending regularization energy automatically weighted by leave-one-out cross-validation. The accuracy of the algorithm is validated on phantom datasets and its clinical interest illustrated on patient datasets by comparing coverage and apposition score maps for registered image volumes.

Keywords: optical coherence tomography, landmark registration, coronary artery stenting

1 Introduction

Optical Coherence Tomography (OCT) is an intravascular imaging technique that provides *in vivo* high-resolution transversal views of coronary artery segments allowing to control the outcome of interventional therapies. It can accurately differentiate the most superficial layers of the arterial wall as well as the stent wire and the vascular tissue surrounding them [1].

OCT appears to be the most efficient technique to confirm correct apposition of a stent mesh immediately after the procedure [2]. OCT can also evaluate the remote implantation of stent neointimal coverage, and corresponding good arterial healing. Finally, during fading of rare thrombotic complications, the high-resolution endoluminal images allow to define the remaining part of obstructive thrombus and its evolution under drug treatment, or after mechanical thrombectomy. In each of those situations, it is important to compare automatic pullbacks obtained at different times on the same arterial segment. Comparative measurements of surfaces and volumes (either of the vessel lumen area, or the media overlying the stent, being a case of neointima or thrombus depending on the context) require accurate registration in longitudinal and axial views. To our knowledge, there is no existing literature on direct OCT to

OCT registration, some works have dealt with its registration to IVUS [3] or with IVUS to IVUS registration [4]. These are 2D iconic registration frameworks based on cross-correlation similarity measure that applies to key frames matched by the user.

The proposed method is also based on anatomical landmarks such as the birth of collateral branches on selected frames, but our contribution is to compute a non-rigid robust transformation between the two OCT pullbacks from the landmarks with a B-spline geometric model comparable to the one used in angio-IVUS or OCT registration frameworks (see for instance [5]). It accounts for the variations in probe trajectory and pullback angular speed. Accuracy of the registration algorithm is assessed using several phantom acquisitions. Score maps of malapposition and neointimal coverage are also compared for registered pullbacks of two patients [10,11].

2 Material and methods

2.1 OCT acquisition protocol

The OCT probe is made of a Michelson interferometer integrated at the tip of a fiber optic segment. The lumen ray is split in two halves. The first half is reflected by the reference mirror and the other half by the coronary artery itself. The state-of-the-art technology (ImageWire C7, LightLab Imaging, Westford, MA) is frequency-domain OCT (FD-OCT) uses the Fourier transform to provide a back reflection profile as a function of depth [6]. The main advantage of OCT over other invasive techniques as IVUS (IntraVascular UltraSound) are improved axial and lateral resolutions up to 12µm and 19µm respectively at a maximum rate of 100 frames per second. Penetration depth and pullback speed are the main limitations of this technology, but they have significantly improved with the FD-OCT generation up to 10mm and 20mm/s respectively. Therefore, a pullback of length L=53.8 mm only takes 2.69s; short enough so that the physiological saline flush, used to make the lumen transparent to red light, can be performed without stopping blood circulation using an occlusive balloon. The OCT final frame stack is made of nsl=268 transversal slices, but, the actual acquisition has a helical geometry (at 100 max RPS and a typical pitch of 0.2mm) that corresponds to the rotation of the probe along the pullback trajectory [6]. As shown by Fig. 1, each frame is computed from the polar to Cartesian transformation of lpf=504 lines per frame (for the C7 system) of one helical helix revolution.

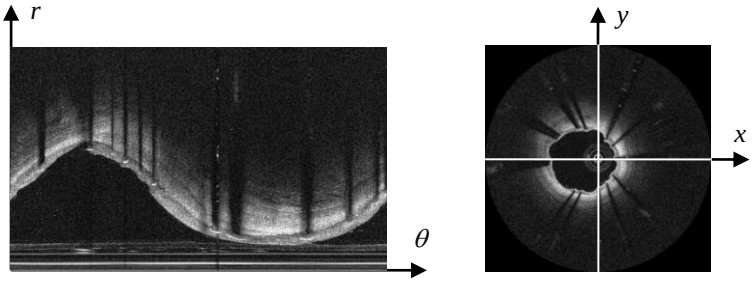

Fig. 1. OCT raw image slice and the corresponding slice after transformation from polar coordinates (r,θ) to Cartesian coordinates (x,y).

2.2 Geometrical transformation between image volumes

As it can be observed in phantom acquisitions (Fig. 2), the differences between the source image volume $S(x,y,z)$ (Fig. 2a) and the target image volume $T(x,y,z)$ (Fig. 2b) are threefold:

- Acquisition pullbacks never start at the same point leading to offsets between slices in longitudinal direction z;
- The position of the acquisition probe with respect to lumen and stent features is not perfectly reproducible due to temporal changes in vessel geometry during cardiac cycle and between acquisitions;
- The angular origins of OCT acquisitions are not in correspondence because they depend on when the acquisitions start. Moreover, angular offsets are likely to occur between two acquisition pullbacks due either to vessel slight torsion during heart contraction, or to temporal changes in friction between the rotating probe and its guide that influences angular speed.

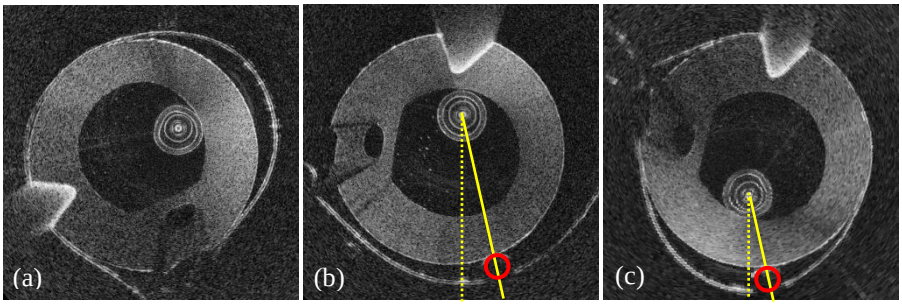

Fig. 2. A given slice of the source (a and c) and target (b) OCT image for the phantom in case of torsion constraint. The source slice before registration (a) shows several discrepancies with regard to the target slice: longitudinal offset of several slices, off-center displacement and variable angular offset. The position of the spherical metallic markers is highlighted by a red circle and yellow lines mark that the angles between markers and vertical direction with respect to the probe are preserved.

The transformation described by the first two points is a translation the vector of which can be interpolated by a 3D nonperiodic B-spline curve of parameter $t \in [0,1]$ and degree p:

$$\Delta\mathbf{P}(t) = \sum_{i=0}^{n} \Delta\mathbf{P_i} N_{i,p}(t), \tag{1}$$

where $\mathbf{\Delta P_i}$ are the $n+1$ control points defined over the non-decreasing sequence of $n+p+2$ knots, $0=t_0=\ldots=t_p<\ldots<t_{n+1}=\ldots=t_{n+p+1}=1$ and $N_{i,p}$ the $n+1$ basis functions of degree p.

The angular offset $\Delta\theta$ of the deformation is also described by a B-spline of parameter t and degree p, sharing the same knot sequence as the curve $\mathbf{\Delta P}(t)$:

$$\Delta\theta(t) = \sum_{i=0}^{n} \Delta\theta_i N_{i,p}(t), \tag{2}$$

where $\Delta\theta_i$ are the n+1 control values defined over the knots.

2.3 Landmark-based Euclidean constraint

The unknowns of the deformation model are the control points $\mathbf{\Delta P_i}$ and the angular control values $\Delta\theta_i$, namely 4 scalars times n+1. One practical way to estimate them is to ask the cardiologist for a few point correspondences between the source and target image volumes.

Usually, for a five-cm long segment, it is feasible to find few invariant features such as bifurcations with small collateral branches. The stent itself and the metallic echoes of its wire, called struts, cannot be used as landmarks because of the impossibility of visually pairing them as they all look like light echoes. With the exception of very specific cases, e.g. the presence of plaque or thrombus with distinctive geometry, there will never be more than 10 landmarks, being the usual case less than 5. Therefore the model must adapt itself to the given number of landmarks: the more landmarks the user provides, the more accurate the description will be. Towards this end n was chosen equal to 10, giving enough degree of freedom to the representation. In the case where there are less landmark constraints than unknowns, additional regularization constraints are mandatory.

In practice, the m landmark points are picked out in the source and target Cartesian coordinate systems, then converted into helical coordinates $\mathbf{S}(t_s,r_s)$ and $\mathbf{T}(t_t,r_t)$, where t is the normalized B-spline parameter (nearly proportional to the curvilinear abscissa given the fact that the curve is almost rectilinear) and r is the distance to the axis curve (Fig. 3).

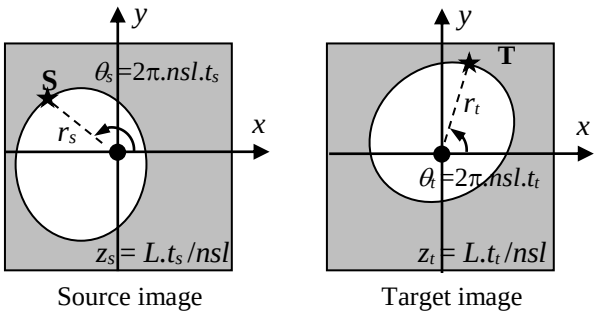

Fig. 3. Schematic view of two paired points **S** and **T** picked out from two slices at respective longitudinal positions z_s and z_t.

The deformation defined by the curve and the angular B-spline model allow transforming target image coordinates to source image coordinates. They can be constrained by the translation vectors $\mathbf{\Delta P}$, and angular offsets $\Delta\theta$, computed at m different target parameter values t_j from the landmark pairs given by the user:

$$\Delta\mathbf{P}(t_j) = \begin{pmatrix} (r_t - r_s)\cos\theta_s \\ (r_t - r_s)\sin\theta_s \\ z_t - z_s \end{pmatrix} \text{ and } \Delta\theta(t_j) = \theta_s - \theta_t \tag{3}$$

Minimizing the distance between the pairs of landmarks turns into finding the control points $\mathbf{\Delta P_i}$ and angular values $\Delta\theta_i$ respectively written in matrix and vector form $\mathbf{\Pi}$ and $\mathbf{\Theta}$ that minimize the data energy terms:

$$\varepsilon_{d\mathrm{P}}(\mathbf{\Pi}) = \|\mathbf{N\Pi} - \mathbf{D}_\mathrm{P}\|^2 \text{ and } \varepsilon_{d\theta}(\mathbf{\Theta}) = \|\mathbf{N\Theta} - \mathbf{D}_\theta\|^2, \tag{4}$$

$$\text{with } \mathbf{N} = \begin{bmatrix} N_{0,p}(t_0) & \cdots & N_{n,p}(t_0) \\ \vdots & N_{i,p}(t_j) & \vdots \\ N_{0,p}(t_m) & \cdots & N_{n,p}(t_m) \end{bmatrix}, \tag{5}$$

$$\mathbf{D}_\mathrm{P}^\mathrm{T} = \begin{bmatrix} \mathbf{\Delta P}(t_0) & \cdots \mathbf{\Delta P}(t_j) \cdots & \mathbf{\Delta P}(t_m) \end{bmatrix} \text{ and } \mathbf{D}_\theta^\mathrm{T} = \begin{bmatrix} \Delta\theta(t_0) & \cdots \Delta\theta(t_j) \cdots & \Delta\theta(t_m) \end{bmatrix}. \tag{6}$$

2.4 Bending energy for regularization

To make the minimization problems of $\varepsilon_{d\mathrm{P}}$ and $\varepsilon_{d\theta}$ well-posed, bending energy terms $\varepsilon_{b\mathrm{P}}$ and $\varepsilon_{b\theta}$ are added to them, and weighted by regularization factors λ_P and λ_θ. They are defined by the integral of the second derivative over the natural domain of the B-splines:

$$\varepsilon_{b\mathrm{P}}(\mathbf{\Pi}) = \int_0^1 \left(\frac{\partial^2 \mathbf{\Delta P}(t)}{\partial t^2}\right)^2 dt \text{ and } \varepsilon_{b\theta}(\mathbf{\Theta}) = \int_0^1 \left(\frac{\partial^2 \Delta\theta(t)}{\partial t^2}\right)^2 dt. \tag{7}$$

In the cubic case (p=3), they can be expressed in matrix form [7]:

$$\varepsilon_{b\mathrm{P}}(\mathbf{\Pi}) = \left|\mathbf{\Pi^T B \Pi}\right|_1 \text{ and } \varepsilon_{b\theta}(\mathbf{\Theta}) = \mathbf{\Theta^T B \Theta}, \tag{8}$$

where $\mathbf{B}$ is a (n+1)×(n+1) matrix, called the bending matrix, built from summing over the diagonal n–3 times the matrix $\mathbf{b}$ of dimensions 4×4 corresponding to the elementary bending over the intervals between successive internal B-spline knots:

$$\mathbf{b} = \begin{bmatrix} 2 & -3 & 0 & 1 \\ -3 & 6 & -3 & 0 \\ 0 & -3 & 6 & -3 \\ 1 & 0 & -3 & 2 \end{bmatrix}. \tag{9}$$

The solution of the regularized problem is given by:

$$\mathbf{\Pi} = \mathbf{H}(\lambda_\mathrm{P})\mathbf{D}_\mathrm{P} = (\mathbf{N}^\mathrm{T}\mathbf{N} + \lambda_\mathrm{P}\mathbf{B}^\mathrm{T}\mathbf{B})^{-1}\mathbf{N}^\mathrm{T}\mathbf{D}_\mathrm{P}, \tag{10}$$

$$\mathbf{\Theta} = \mathbf{H}(\lambda_\theta)\mathbf{D}_\theta = (\mathbf{N}^\mathrm{T}\mathbf{N} + \lambda_\theta\mathbf{B}^\mathrm{T}\mathbf{B})^{-1}\mathbf{N}^\mathrm{T}\mathbf{D}_\theta. \tag{11}$$

The hyperparameters λ_P and λ_θ are estimated using the leave-one-out cross-validation criterion defined in [8] that has been proved to have a closed-form solution in case of linear least-square problem:

$$\mathrm{LOOCV}(\lambda_P) = \frac{1}{n}\left\|\mathrm{diag}\left(\frac{1}{\mathbf{1}-\mathrm{diag}(\mathbf{H}(\lambda_P))}\right)(\mathbf{N\Pi}-\mathbf{D}_P)\right\|^2, \quad (12)$$

$$\mathrm{LOOCV}(\lambda_\theta) = \frac{1}{n}\left\|\mathrm{diag}\left(\frac{1}{\mathbf{1}-\mathrm{diag}(\mathbf{H}(\lambda_\theta))}\right)(\mathbf{N\Theta}-\mathbf{D}_\theta)\right\|^2. \quad (13)$$

As a first approximation, these functions are minimized using the Powell's conjugate gradient descent algorithm [9]. Global search appears also as a sensible approach since local minima could arise as the function is not perfectly convex.

2.5 Helical ray casting for source image deformation

Simulated rays were sampled along the estimated 3D curve. They served as support for the target image voxels, and are stuck into the source image volume. As target voxels usually do not fall onto the grid of source voxels, a trilinear interpolation scheme was used to compute approximate gray levels. For the C7 OCT system, the number of rays is $n_r = nsl \times lpf$ =135,072. Ray number k corresponds to the parameter $t_s = k/n_r$ and to the normal pullback rotation angle value of $\theta_s = 2\pi.nsl.t_s$ with an offset equal to $\Delta\theta(t_s)$.

2.6 Validation

To validate the registration algorithm, two kinds of OCT data were used:

- A simple phantom was build using a urinary probe injected with water in order to adjust optical indices at the lumen wall. Six experiments were carried out: from 5 to 16 small metallic balls of diameter 0.6 mm evenly and non evenly spread were stuck outside the probe using adhesive tape. Different amounts of bending and/or torsion of the probe were manually induced between the two OCT acquisitions in order to mimic the constraints imposed by coronary artery deformation during the cardiac cycle. One half of the markers were used as landmarks for registration and the other half as test points to assess the accuracy of the process.
- Two datasets of patient OCT sequences, the first before and after stent apposition correction during the same implantation procedure, and the second before and after stent neointimal coverage at 3 months delay. A comparison between apposition and coverage score maps with respect to the same referential after registration was made. The way cylindrical maps are obtained is fully detailed in [10,11].

3 Experimental results and discussion

Figure 2 shows good visual correspondence between the target slice (b) and the source slice after deformation (c).

The landmarks are perfectly superimposed as confirmed by the distance between test markers that decreases from (8.29±2.53) mm before registration to (0.34±0.30) mm after registration (1.5 order of magnitude of the interslice resolution). The error is

inversely proportional to the number of constraint points used, ranging from 0.81 mm (3 points) to 0.11 mm (10 points). As expected, the spacing between points influences results, by increasing the error when points are non evenly spread (up to 0.9mm in our case for 3 points with the second not in the middle). Certainly with one landmark in a given slice, only the angle between the marker itself and the probe can be recovered exactly, and small errors in object orientation may occur if the probe moves with respect to the vessel. The phantom case of Fig. 2 is one of the most pejorative cases as the probe has moved in the opposite diametrical direction due to the imposed torsion deformation. Nevertheless, the result is accurate enough and visually consistent in the opinion of the cardiologist.

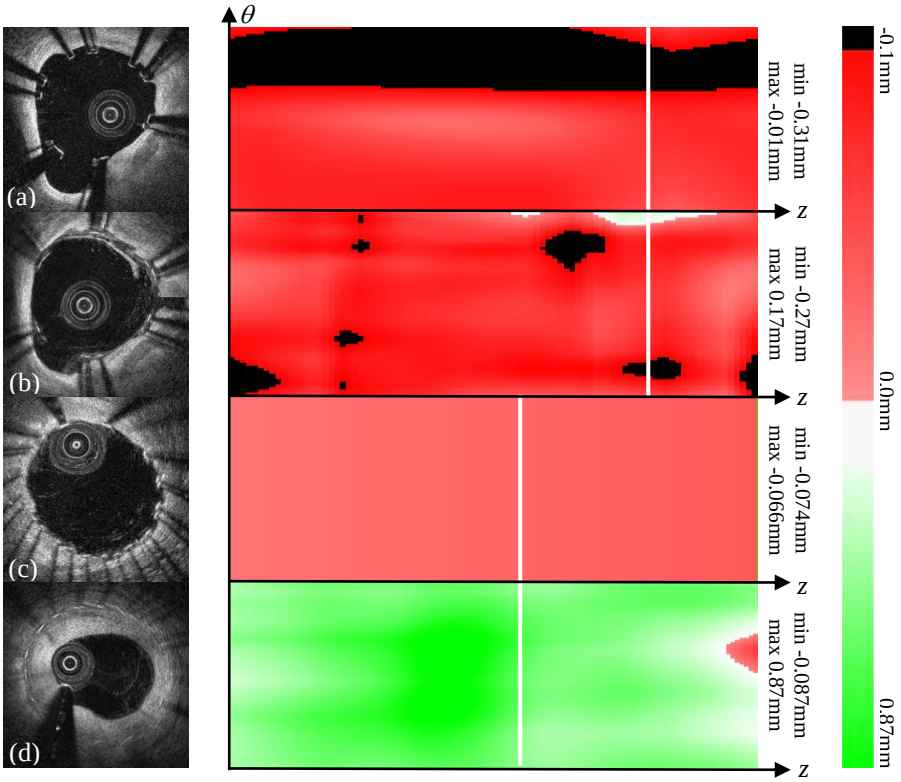

Fig. 4. Comparison of registered slices and score maps in cylindrical coordinates (z, θ) of the distance between stent and lumen wall (ill-placed stent in black, perfectly apposed but naked stent in red and covered stent with increasing thickness in green levels): before (a) and after (b) malapposition correction and before (c) and after (d) stent coverage. The white vertical lines indicate the location of the selected slices. Minimum and maximal distances between stent and lumen walls are given for the four color maps (negative if the strut echo lies inside the lumen).

Another major benefit of this kind of transformation is that it perfectly matches score maps built in cylindrical coordinates. As shown in figure 4, it is possible to compute distance maps between stent and lumen wall, and to compare them point by point, thanks to the performed registration. Distance greater than the mesh thickness, defines an ill-placed stent in black. Figures 4(a) and (b) show that post-dilatation has

significantly enhanced stent apposition and that only a few residual black spots remain. Figures 4(c) and (d) show the evolution between a very homogeneous apposition distance map to a very important and heterogeneous restenosis map in only 3 months. For patient data, distance errors computed at the landmarks were (11.1±2.1) mm before registration and (0.15±0.12) mm after registration.

Registration of a 976×504×268 raw target OCT volume with a 976×976×268 cartesian source OCT volume takes about one minute. The present software was implemented in C++ using ITK (Kitware Inc., New York, USA). The major computational cost stands in the ray casting process that is for now implemented in a multithreaded way but on CPU. Speed would be greatly increased if 3D texture capabilities on GPU were used.

4 Conclusion and perspectives

An accurate landmark-based method to superimpose OCT image sequences was described; it is based on a few landmarks pointed out by the cardiologist. Comparative analysis based on this registration algorithm will allow for extensive studies targetting tissue repair process in the vicinity of the stent, and also evaluate the impact of corrective treatments such as thrombo-aspiration after thrombotic occlusion or post-dilatation in case of suboptimal initial deployment.

References

1. T.L. Pinto and R. Waksman. Clinical applications of optical coherence tomography. *Journal of Interventional Cardiology*, 19:566-573, 2006.
2. F. Prati, E. Regar, G.S. Mintz et al. Expert review document on methodology, terminology, and clinical applications of optical coherence tomography: physical principles, methodology of image acquisition, and clinical application for assessment of coronary arteries and atherosclerosis, *European Heart Journal*, 31(4):401-415, 2010.
3. G. Unal, S. Lankton, S. Carlier, G. Slabaugh and Y. Chen. Fusion of IVUS and OCT through semi-automatic registration, in *Proc. International Workshop on Computer Vision for Intravascular Imaging* (CVII), pp. 163-170, 2006
4. J. Amores and P. Radeva. Non-rigid registration of vessel structures in IVUS images, Ib-PRIA 2003, LNCS 2652, pp. 45–52, 2003.
5. B. Godbout, J.A. de Guise, G. Soulez and G. Cloutier. 3D registration of vessel structures from IVUS data on biplane angiography, *Academic Radiology*, 12(1):10-16, 2005.
6. M. E. Brezinski. Optical Coherence Tomography: principles and applications. Burlington, MA: Elsevier, 2006.
7. F. Brunet. Contributions to parametric image reconstruction and 3D surface reconstruction, PhD thesis, 2011.
8. A. Bartoli. Maximizing the predictivity of smooth deformable image warps through cross-validation. *Journal of Mathematical Imaging and Vision*, 31(2-3):133–145, 2008.
9. M.J.D. Powell. An efficient method for finding the minimum of a function of several variables without calculating derivatives. *Computer Journal*, 7:155–162, 1964.
10. F. Dubuisson, C. Kauffmann, P. Motreff, L. Sarry. In vivo OCT coronary imaging augmented with stent reendothelialization score, MICCAI 2009, Part I, LNCS 5761:475–482, 2009.
11. C. Kauffmann, P. Motreff, L. Sarry. In vivo supervised analysis of stent reendothelialization from Optical Coherent Tomography. *IEEE Trans. Medical Imaging*, 29:807–819, 2010.